CRAHCN-O: A Consistent Reduced Atmospheric Hybrid Chemical Network Oxygen Extension for Hydrogen Cyanide and Formaldehyde Chemistry in CO_2-, N_2-, H_2O-, CH_4-, and H_2-Dominated Atmospheres

Ben K. D. Pearce,[1,*] Paul W. Ayers,[2] and Ralph E. Pudritz[1]

[1] *Origins Institute and Department of Physics and Astronomy, McMaster University, ABB 241, 1280 Main St, Hamilton, ON, L8S 4M1, Canada*

[2] *Origins Institute and Department of Chemistry and Chemical Biology, McMaster University, ABB 156, 1280 Main St, Hamilton, ON, L8S 4M1, Canada*

Abstract: Hydrogen cyanide (HCN) and formaldehyde (H_2CO) are key precursors to biomolecules such as nucleobases and amino acids in planetary atmospheres; However, many reactions which produce and destroy these species in atmospheres containing CO_2 and H_2O are still missing from the literature. We use a quantum chemistry approach to find these missing reactions and calculate their rate coefficients using canonical variational transition state theory and Rice–Ramsperger–Kassel–Marcus/master equation theory at the BHandHLYP/aug-cc-pVDZ level of theory. We calculate the rate coefficients for 126 total reactions, and validate our calculations by comparing with experimental data in the 39% of available cases. Our calculated rate coefficients are most frequently within an factor of 2 of experimental values, and generally always within an order of magnitude of these values. We discover 45 previously unknown reactions, and identify 6 from this list that are most likely to dominate H_2CO and HCN production and destruction in planetary atmospheres. We highlight $^1O + CH_3 \longrightarrow H_2CO + H$ as a new key source, and $H_2CO + {}^1O \longrightarrow HCO + OH$ as a new key sink, for H_2CO in upper planetary atmospheres. In this effort, we develop an oxygen extension to our consistent reduced atmospheric hybrid chemical network (CRAHCN-O), building off our previously developed network for HCN production in N_2-, CH_4- and H_2-dominated atmospheres (CRAHCN). This extension can be used to simulate both HCN and H_2CO production in atmospheres dominated by any of CO_2, N_2, H_2O, CH_4, and H_2.

INTRODUCTION

Hydrogen cyanide (HCN) and formaldehyde (H_2CO) are key precursors to various biomolecules required for the origin of life. The four nucleobases in RNA, i.e., adenine, guanine, cytosine and uracil, form in aqueous solutions containing one or both of these reactants[1–3]. Ribose, which pairs with phosphate to make up the backbone of RNA, forms from the oligomerization of H_2CO[4,5]. Amino acids form via Strecker synthesis, which includes both HCN and an aldehyde (H_2CO for glycine) as reactants[6,7].

Given their substantial role in producing biomolecules, HCN and H_2CO may be distinguishing atmospheric features of what we call *biogenic worlds*. These are worlds capable of producing key biomolecules rather than requiring they be delivered (e.g., by meteorites). It is presently unknown whether the early Earth was biogenic.

The redox state of the oldest minerals on the planet suggests the early Earth atmosphere was composed of "weakly reducing" gases, i.e., CO_2, N_2, and H_2O, with relatively smaller amounts of CH_4, CO, and H_2[8,9]. These atmospheric species are broken up into reactive radicals by UV radiation, lightning, and/or galactic cosmic rays (GCRs), which allows disequilibrium chemistry and the production of HCN and H_2CO to occur[8,10]. The following pathways are possible from the dissociation of these "weakly reducing" species[11–15]:

$$CO_2 + h\nu \longrightarrow CO + {}^3O \tag{1}$$

$$\longrightarrow CO + {}^1O \tag{2}$$

$$N_2 + h\nu \longrightarrow {}^4N + {}^2N \tag{3}$$

$$CH_4 + h\nu \longrightarrow CH_3 + H \tag{4}$$

$$\longrightarrow {}^3CH_2 + 2\,H \tag{5}$$

$$\longrightarrow {}^1CH_2 + H_2 \tag{6}$$

$$\longrightarrow CH + H_2 + H \tag{7}$$

$$H_2O + h\nu \longrightarrow OH + H \tag{8}$$

$$H_2 + h\nu \longrightarrow 2\,H \tag{9}$$

where the superscripts, ^{1}, ^{2}, ^{3}, and ^{4} refer to the singlet, doublet, triplet and quartet electronic spin states.

* Corresponding author:pearcbe@mcmaster.ca

One way to better understand the biogenicity of the early Earth, is to use chemical kinetic models to simulate the production of HCN and H_2CO in plausible early Earth atmospheres. Atmospheric simulations of these species for primitive Earth conditions have been performed in the past[10,16,17], which make use of collections of reaction rate coefficients typically gathered from various sources the literature (e.g. experiment, theoretical simulations, thermodynamics, similar reactions).

The literature, however, is still missing several reactions between the radicals produced in CO_2-, N_2-, H_2O-, CH_4-, and H_2-dominated atmospheres, and these reactions may be crucial to understanding HCN and H_2CO chemistry in early Earth and other terrestrial environments. The largest gap in rate coefficient data is for reactions involving electronically excited species, e.g. ^1O, ^2N, and $^1CH_2$, which are directly produced from the dissociation of CO_2, N_2, and CH_4, respectively.

In Pearce et al.[18] and Pearce et al.[19], we developed an accurate and feasible method making use of computational quantum chemistry coupled with canonical variational transition state theory (CVT)[20] and Rice–Ramsperger–Kassel–Marcus/master equation (RRKM/ME) theory[21] to calculate a large network of reaction rate coefficients for one-, two- and three-body reactions. We first used this method to explore the entire field of possible reactions for a list of primary species in N_2-, CH_4-, and H_2-dominated atmospheres, and uncovered 48 previously unknown reactions; many of which were based on excited species such as ^2N and $^1CH_2$. We then built an initial reduced network of 104 reactions based on this exploratory study, and used it to simulate HCN production in Titan's atmosphere[18]. This approach provided us with a more complete picture of HCN chemistry on Titan, as one of our newly discovered reactions was found to be one of the four dominant channels to HCN production on Titan[18].

In this work, we use the same theoretical approach to expand upon our initial network, by exploring and calculating all the potential reactions between three key oxygen species present on the early Earth (CO_2, H_2O, H_2CO), their dissociation radicals (CO, ^3O, ^1O, OH, and HCO), and all the non-oxygen primary species in our network (see Table 1 for the list of primary species). In this effort, we discover 45 brand new reactions, which are mainly based on HCO, H_2CN, ^1O, ^2N, $^1CH_2$, and CH. We calculate the rate coefficients for a total of 126 reactions, and validate our calculations by comparing with experimental data in the 39% of available cases.

Finally, we build the consistent reduced atmospheric hybrid chemical network oxygen extension (CRAHCN-O), composed of experimental rate coefficients when available, and our calculated values otherwise. CRAHCN-O is the amalgamation of the network developed in Pearce et al.[18], and the oxygen reactions explored in this work. This network can be used to accurately simulate HCN and H_2CO production in CO_2-, N_2-, H_2O-, CH_4-, and H_2-dominated atmospheres.

The paper is outlined as follows: In the Methods section, we detail the theoretical and computational approach we use to explore reactions and calculate their rate coefficients. In the Results section, we describe the results of our rate coefficient calculations, including their agreement with any available experiments. We also discuss the limitations of our theoretical approach. In the Discussion section, we highlight 6 new reactions from this work which are potentially key production and destruction pathways to H_2CO and HCN in planetary atmospheres. We also summarize CRAHCN-O and describe how it can be used for other atmospheric models. Finally, in the Conclusions section, we summarize the main conclusions from this work.

The Supporting Information (SI) contains two tables summarizing the new CRAHCN-O rate coefficient data (the non-oxygen reaction data can be found in Pearce et al.[18]), any experimental rate coefficient data for reactions calculated in this work, the Lennard-Jones parameters used for three-body reaction rate coefficient calculations, a breakdown of some of the non-standard reaction calculations, and the quantum chemistry data used in our calculations.

METHODS

There are four phases to this work: First we explore all the potential reactions between eight oxygen species (CO_2, CO, ^3O, ^1O, H_2O, OH, H_2CO, and HCO) and the primary species in Table 1. These species are the the dominant sources of oxygen in the early Earth atmosphere (CO_2 and H_2O), a key biomolecule precursor (H_2CO) and their dissociation radicals. In this process, we characterize 81 known reactions and discover 45 previously unknown reactions. Second, we calculate the rate coefficients for every reaction that we find at 298 K, and validate the calculations by comparing to experimental data when available (in 39% of cases). Third, we calculate the temperature dependencies for the reactions that have no experimental measurements and have barriers (i.e. strong temperature dependencies from 50–400 K). Last, we gather the experimental and theoretical rate coefficients into the consistent reduced atmospheric hybrid chemical network oxygen extension (CRAHCN-O), which contains experimental values when available, and our calculated rate coefficients otherwise.

Computational Quantum Method and Basis Set

All exploration and rate coefficient calculations are performed with the Becke-Half-and-Half-Lee-Yang-Parr[1]

[1]This hybrid functional uses 50% Hartree-Fock (HF) and 50% density functional theory (DFT) for the exchange energy calculation,

TABLE 1. List of primary molecular species involved in this study and their spin states. Reactions strictly between non-oxygen species (below center line) were explored in Pearce et al. [18] and Pearce et al. [19]. Reactions involving the oxygen species (above center line) are new to this study.

Species	Spin state	Ground/Excited state
CO_2	singlet	ground
H_2CO	singlet	ground
HCO	doublet	ground
CO	singlet	ground
H_2O	singlet	ground
OH	doublet	ground
^3O	triplet	ground
^1O	singlet	excited
H_2CN	doublet	ground
HCN	singlet	ground
CN	doublet	ground
N_2	singlet	ground
NH	triplet	ground
^2N	doublet	excited
^4N	quartet	ground
CH_4	singlet	ground
CH_3	doublet	ground
$^1CH_2$	singlet	excited
$^3CH_2$	triplet	ground
CH	doublet	ground
H_2	singlet	ground
H	doublet	ground

(BHandHLYP) density functional and the augmented correlation-consistent polarized valence double-ζ (aug-cc-pVDZ) basis set[22–26].

We have four key reasons for choosing this level of theory to perform our calculations:

1) We have benchmarked BHandHLYP/aug-cc-pVDZ rate coefficient calculations by comparing with experimental values in the past, and this method most frequently provides the best accuracy with respect to agreement with experimental values in comparison with other widely used, computationally cost effective methods.

In Pearce et al. [18], we compared the accuracy of 3 methods for calculating 12 reaction rate coefficients. We found BHandHLYP/aug-cc-pVDZ rate coefficient calculations give the best, or equal to the best agreement with experiment in 8 out of 12 cases. This is compared to ωB97XD/aug-cc-pVDZ and CCSD/aug-cc-pVTZ, which gave the best, or equal to the best agreement with experiment in 7 out of 12 and 6 out of 12 cases, respectively[18]. In another method-comparison study on a single reaction between BHandHLYP, CCSD, CAM-B3LYP, M06-2x, B3LYP and HF, all with the aug-cc-pVDZ basis set, we found that only BHandHLYP and CAM-B3LYP provide rate coefficients within the experimental range[19].

2) BHandHLYP/aug-cc-pVDZ calculations paired with CVT and RRKM/ME theory typically compute rate coefficients within a factor of two of experimental values, and all calculations generally fall within an order of magnitude of experimental values. This accuracy is consistent with typical uncertainties assigned in large-scale experimental data evaluations[27,28].

For examples in our network, Baulch et al. [27] assign uncertainties of 2–3 to $HCO + HCO \longrightarrow H_2CO + CO$ and $^3O + CH \longrightarrow CO + H$ and order-of-magnitude uncertainties to $CO_2 + CH \longrightarrow$ products, $H_2O + CH \longrightarrow$ products, and $H_2CO + CH \longrightarrow$ products.

3) BHandHLYP/aug-cc-pVDZ calculations are computationally cost effective, and therefore feasible for a large scale exploratory study such as ours.

We have also shown in previous work for 12 rate coefficients, that increasing the basis set to the more computationally expensive aug-cc-pVTZ level does not increase the accuracy of our calculations with respect to agreement with experimental values[18].

4) Finally, using the BHandHLYP/aug-cc-pVDZ level of theory for all the calculations in this oxygen extension allows us to maintain consistency with the calculations in the original network (CRAHCN[18]).

offering a compromise between HF, which tends to overestimate energy barriers, and DFT, which tends to underestimate energy barriers.

Reaction Exploration

Using the Gaussian 09 software package[29], we perform a thorough search for reactions between eight oxygen

species (CO_2, CO, ^3O, ^1O, H_2O, OH, H_2CO, and HCO) and the 22 primary species in this study (see Table 1). The procedure below is carried out for $8\times22 = 176$ pairs of species.

Using the Avogadro molecular visualization software[30,31], we placed each species at a handful of different distances and orientations form its reaction partner. We use a bit of chemical intuition when determining the distance between the species, e.g., abstraction reactions in our network tend to occur at short separations (1–2 $\mathring{A}$), whereas addition reactions tend to be longer range (2–6 $\mathring{A}$).

We then copy the geometries into Gaussian input files, and use the 'opt=modredundant' option to freeze the bond distances between one atom of each species. We run the Gaussian simulations with vibrational analyses to allow us to identify whether points along the MEP were found. A point along a MEP is identified by a single negative frequency that oscillates in the direction of the reaction. We run multiple simulations to look for possible abstraction, addition, and bond insertion reactions. For reactions that form a single product, we continue the exploration of that product by searching for efficient decay and/or isomerization pathways. In many cases, we find the product efficiently decays into other products, sometimes after one or more isomerizations.

For cases where our above approach fails to find a MEP, we have developed a Python program that can be used to perform a more thorough scan of the potential energy surface. This program takes two species geometries as input, selects, e.g., 10 random separations and orientations for those species, and runs those Gaussian simulations in parallel. This program is especially useful for MEPs that turn out to be not strictly intuitive (e.g. $OH + {}^1CH_2$).

Once we find a point along a MEP, we then characterize the reaction path by doing a coarse-grain scan backwards and forwards from the identified point in intervals of $0.1\mathring{A}$. We then plot the Gibbs free energies of these optimized points along the reaction path, and analyze the points using Avogadro to find the rough location(s) of the transition state(s). In several cases we find more than one transition state along a reaction path, with one or more stable structures between the reactants and the products.

Rate coefficient calculations

One- and Two-body Reactions

We calculate one- and two-body reaction rate coefficients using canonical variational transition state theory (CVT). This is a statistical mechanics approach which makes use of the canonical ensemble. This method can be used to calculate rate coefficients for reactions with and without energy barriers[20].

CVT can be explained as follows. There is a point that is far enough along the minimum energy reaction path (MEP), that the reactants that cross over this point are unlikely to cross back. This point is defined as the location where the generalized transition state (GT) rate coefficient is at its smallest value, therefore providing best dynamical bottleneck[20]. This is expressed as:[32]

$$k_{CVT}(T,s) = \min_s \{k_{GT}(T,s)\}\,. \tag{10}$$

where $k_{GT}(T,s)$ is the generalized transition state theory rate coefficient, T is the temperature, and s is a point along the MEP (e.g. bond distance).

To find the location along the MEP where the rate coefficient is at a minimum, we use the maximum Gibbs free energy criterion[32,33]. It can be seen from the quasi-thermodynamic equation of transition-state theory that the maximum value for $\Delta G_{GT}(T,s)$ corresponds to a minimum value for $k_{GT}(T,s)$.

$$k_{GT}(T,s) = \frac{k_B T}{h} K^0 e^{-\Delta G_{GT}(T,s)/RT}, \tag{11}$$

where K^0 is the reaction quotient under standard state conditions (i.e. 1 cm^3 for second-order reactions, 1 cm^6 for third-order reactions), and $\Delta G_{GT}(T,s)$ is the difference in the Gibbs free energy between transition state and reactants (kJ mol^{-1}).

This method offers a compromise of energetic and entropic effects, as ΔG contains both enthalpy and entropy[32,33]. To obtain a similar accuracy for all calculations, we refine our coarse grain scans near the Gibbs maxima to a precision of 0.01 $\mathring{A}$.

The generalized transition state theory rate coefficient, neglecting effects due to tunneling, can be calculated with the equation[32,34]

$$k_{GT}(T,s) = \sigma \frac{k_B T}{h} \frac{Q^{\ddagger}(T,s)}{\prod_{i=1}^{N} Q_i^{n_i}(T)} e^{-E_0(s)/RT}. \tag{12}$$

where σ is the reaction path multiplicity, k_B is the Boltzmann constant (1.38×10^{-23} J K^{-1}), T is temperature (K), h is the Planck constant (6.63×10^{-34} J·s), $Q^{\ddagger}$ is the partition function of the transition state per unit volume (cm^{-3}), with its zero of energy at the saddle point, Q_i is the partition function of species i per unit volume, with its zero of energy at the equilibrium position of species i, n_i is the stoichiometric coefficient of species i, N is the number of reactant species, E_0 is the difference in zero-point energies between the generalized transition state and the reactants (kJ mol^{-1}) (0 for barrierless reactions), and R is the gas constant (8.314×10^{-3} kJ K^{-1} mol^{-1}).

The partition functions per unit volume have four components and are gathered from the Gaussian output files,

$$Q = \frac{q_t}{V} q_e q_v q_r. \tag{13}$$

where V is the volume (cm^{-3}) and the t, e, v, and r subscripts stand for translational, electronic, vibrational, and rotational, respectively.

In some cases, there are multiple steps (i.e. transition states) to a single reaction, and we must use mechanistic modeling in order to determine the steady-state solution of the overall rate equation. We place an example of a mechanistic model in Case Study 9 in the SI.

Three-body reactions

In the cases where two reactants form a single product, a colliding third body is required to remove excess vibrational energy from the product to prevent it from dissociating[35]. This is expressed as,

$$A + B \longrightarrow C_{(\nu)} \tag{14}$$

$$C_{(\nu)} \xrightarrow{+M} C. \tag{15}$$

The rate coefficient for these three-body reactions is expressed as[36]:

$$k([M]) = \frac{k_0[M]/k_\infty}{1 + k_0[M]/k_\infty} k_\infty \tag{16}$$

where k_0 is the third-order low-pressure limit rate coefficient (cm^6s^{-1}), [M] is the number density of the colliding third body, and k_∞ is the second-order high-pressure limit rate coefficient (cm^3s^{-1}).

The high-pressure limit rate coefficients are equivalent to the two-body reaction rate coefficients (i.e., A + B $\longrightarrow$ C), and can be calculated using CVT as above. We make use of the ktools code of the Multiwell Program Suite for the high pressure limit rate coefficient calculations[37–39].

The low-pressure limit rate coefficients, on the other hand, require information about the collisional third body for their calculation. To calculate these values, we use the Multiwell Master Equation (ME) code, which employs RRKM theory. The ME contains the probabilities that the vibrationally excited product will be stabilized by a colliding third body[40]. Multiwell employs Monte Carlo sampling of the ME to build up a statistical average for the two outcomes of the reaction (i.e., destabilize back into reactants, or stabilize the product).

With the output from these stochastic trials, we calculate the low-pressure limit rate coefficient with the following equation[38,41]:

$$k_0([M]) = \frac{k_\infty f_{prod}}{[M]} \tag{17}$$

where k_∞ is the high-pressure limit rate coefficient, f_{prod} is the fractional yield of the collisionally stabilized product, and [M] is the simulation number density (cm^{-3}), which we lower until k_0 converges.

We simulate three-body reactions using three different colliding bodies, corresponding to potential dominant species in the early Earth atmosphere (N_2, CO_2, and H_2). The energy transfer was treated with a standard exponential-down model with $< \Delta E >_{down} = 0.8$ T K^{-1} cm^{-1}[42,43]. The Lennard-Jones parameters for the bath gases and all the products were taken from the literature[44–46] and can be found in Table S4.

In some cases, when two reactants come together to form a single product, the vibrationally excited product preferably decays along a different channel into something other than the original reactants (e.g. $^1O + H_2 \longrightarrow H_2O_{(\nu)}\cdot \longrightarrow OH + H$). In these cases, we also include the second-order reactions to these favourable decay pathways in our network. We verify the preferred decay pathways of vibrationally excited molecules by looking at previous experimental studies.

Temperature dependencies

For the one- and two-body reactions in this study with barriers, and no experimental measurements, we calculate temperature dependencies for the rate coefficients in the 50–400 K range. Barrierless reaction rate coefficients do not typically vary by more than a factor of ∼3 between 50 and 400 K[47–51]. To obtain temperature dependencies, we calculate the rate coefficients at 50, 100, 200, 298.15, and 400 K and fit the results to the modified Arrhenius expression

$$k(T) = \alpha \left(\frac{T}{300}\right)^\beta e^{-\gamma/T}, \tag{18}$$

where $k(T)$ is the temperature-dependent second-order rate coefficient (cm^3s^{-1}), α, β, and γ are fit parameters, and T is temperature (in K).

RESULTS

Comparison with Experiments

In Table 2 we display the three-body high- and low-pressure limit calculated rate coefficients at 298 K. Out of these 31 reactions, 12 have experimentally measured high-pressure limit rate coefficients. For the low-pressure limit rate coefficients, 9 of the 31 reactions have experimental measurements; However, the bath gases used in the low-pressure experiments often differ from the colliding third bodies in our calculations (i.e. N_2, CO_2, and H_2). When using several different bath gases, low-pressure limit rate coefficients tend to range by ∼ an order of magnitude[27,52–54].

TABLE 2: Lindemann coefficients for the three body reactions in this paper, calculated at 298 K, and valid within the 50–400 K temperature range. k_∞ and k_0 are the third-order rate coefficients in the high and low pressure limits, with units cm^3s^{-1} and cm^6s^{-1}, respectively. These values are for usage in the pressure-dependent rate coefficient equation $k = \frac{k_0[M]/k_\infty}{1+k_0[M]/k_\infty}k_\infty$. Calculations are performed at the BHandHLYP/aug-cc-pVDZ level of theory. Low-pressure limit rate coefficients are calculated for three different bath gases (N_2, CO_2, and H_2). Reactions with rate coefficients slower than $k_\infty = 10^{-13}$ cm^3s^{-1} are not included in this network. The error factor is the multiplicative or divisional factor from the nearest experimental or suggested value.

No.	Reaction equation	k_∞(298) calc.	k_∞(298) exp.	Error$_\infty$	k_0(298) calc.	k_0(298) exp.	Error$_0$
*1.	$CO_2 + {}^1O + M \longrightarrow CO_3 + M$	3.8×10^{-11}	0.1–23$\times10^{-11}$	1	(M=N_2) 3.0×10^{-29} (CO_2) 3.1×10^{-29} (H_2) 6.7×10^{-29}		
*2.	$HCO + {}^2N + M \longrightarrow$ $HCON\cdot + M\cdot \longrightarrow HCNO + M$	2.0×10^{-11}			(N_2) 5.0×10^{-30} (CO_2) 5.6×10^{-30} (H_2) 9.7×10^{-30}		
*3.	$HCO + CH_3 + M \longrightarrow CH_3CHO + M$	5.7×10^{-12}	6.3–44$\times10^{-12}$	1	(N_2) 5.3×10^{-27} (CO_2) 6.4×10^{-27} (H_2) 1.2×10^{-27}		
4.	$HCO + H + M \longrightarrow H_2CO + M$	4.9×10^{-11}			(N_2) 7.4×10^{-30} (CO_2) 9.5×10^{-30} (H_2) 1.4×10^{-29}		
*5.	$CO + CN + M \longrightarrow NCCO + M$	6.0×10^{-12}			(N_2) 6.2×10^{-31} (CO_2) 6.8×10^{-31} (H_2) 1.3×10^{-30}		
6.	$CO + {}^1O + M \longrightarrow CO_2 + M$	2.8×10^{-11}	0.3–7$\times10^{-11}$	1	(N_2) 2.8×10^{-30} (CO_2) 3.0×10^{-30} (H_2) 5.9×10^{-30}	(CO_2) 2.8×10^{-29} ” ”	10 9 5
*7.	$CO + {}^1CH_2 + M \longrightarrow CH_2CO + M$	1.3×10^{-11}			(N_2) 1.7×10^{-28} (CO_2) 1.9×10^{-28} (H_2) 3.3×10^{-28}		
8.	$CO + CH + M \longrightarrow HCCO + M$	4.6×10^{-11}	0.5–17$\times10^{-11}$	1	(N_2) 1.2×10^{-29} (CO_2) 1.3×10^{-29} (H_2) 2.4×10^{-29}	(Ar,He) 2.4–4.1$\times10^{-30}$ ” ”	3 3 6
9.	$CO + H + M \longrightarrow HCO + M$	2.7×10^{-12}			(N_2) 1.8×10^{-33} (CO_2) 2.1×10^{-33} (H_2) 3.4×10^{-33}	(Ne,H_2) 0.5–3.3$\times10^{-34}$ (CO,H_2) 0.8–3.3$\times10^{-34}$ (H_2) 0.8–3.3$\times10^{-34}$	5 6 10
*10.	$OH + H_2CN + M \longrightarrow H_2CNOH + M$	6.9×10^{-12}	6.0×10^{-12}	1	(N_2) 6.5×10^{-30} (CO_2) 7.4×10^{-30} (H_2) 1.3×10^{-29}		
*11.	$OH + CN + M \longrightarrow HOCN + M$	1.0×10^{-12}			(N_2) 2.7×10^{-30} (CO_2) 2.9×10^{-30} (H_2) 5.1×10^{-30}		
12.	$OH + OH + M \longrightarrow H_2O_2 + M$	2.3×10^{-11}	1.5–6.5$\times10^{-11}$	1	(N_2) 4.9×10^{-32} (CO_2) 5.5×10^{-32} (H_2) 9.9×10^{-32}	(N_2) 5.1–330$\times10^{-32}$ (CO_2) 6.4–420$\times10^{-32}$ (He,H_2O) 1.3–1800$\times10^{-32}$	1 1 1
*13.	$OH + {}^3O + M \longrightarrow HO_2 + M$	7.4×10^{-11}			(N_2) 8.5×10^{-32} (CO_2) 9.4×10^{-32} (H_2) 1.8×10^{-31}		
*14.	$OH + {}^1O + M \longrightarrow HO_2 + M$	1.0×10^{-9}			(N_2) 4.1×10^{-30}		

					(CO_2) 4.5×10^{-30} (H_2) 8.3×10^{-30}		
15.	$OH + NH + M \longrightarrow OH\cdots NH\cdot + M\cdot \longrightarrow$ trans$-HNOH + M$	7.0×10^{-12}			(N_2) 8.5×10^{-31} (CO_2) 9.2×10^{-31} (H_2) 1.7×10^{-30}		
16.	$OH + CH_3 + M \longrightarrow OH\cdots CH_3\cdot + M\cdot \longrightarrow CH_3OH + M$	2.0×10^{-11}	9.3–17$\times10^{-11}$	5	(N_2) 2.1×10^{-27} (CO_2) 2.3×10^{-27} (H_2) 3.8×10^{-27}	(He,SF_6) 2.0–7.2$\times10^{-27}$ ” ”	1 1 1
17.	$OH + H + M \longrightarrow H_2O + M$	2.4×10^{-10}			(N_2) 3.0×10^{-31} (CO_2) 3.7×10^{-31} (H_2) 5.1×10^{-31}	(N_2) 4.8–6.8$\times10^{-31}$ (CO_2) 9.0×10^{-31} (He,H_2O) 1.5–6.8$\times10^{-31}$	2 2 1
*18.	$^3O + CN + M \longrightarrow NCO + M$	7.1×10^{-12}	9.4–16$\times10^{-12}$	1	(N_2) 1.3×10^{-30} (CO_2) 1.5×10^{-30} (H_2) 2.6×10^{-30}		
19.	$^3O + {}^3O + M \longrightarrow O_2 + M$	1.8×10^{-11}			(N_2) 3.0×10^{-34} (CO_2) 3.2×10^{-34} (H_2) 6.1×10^{-34}	(N_2) 3.1–10$\times10^{-33}$ (Ar, O_2) 3.9–100$\times10^{-34}$ (Ar, N_2) 3.9–100$\times10^{-34}$	10 1 1
20.	$^3O + {}^4N + M \longrightarrow NO + M$	6.6×10^{-11}			(N_2) 1.6×10^{-33} (CO_2) 1.8×10^{-33} (H_2) 3.3×10^{-33}	(N_2) 5–11$\times10^{-33}$ (CO_2) 1.8×10^{-32} (He, N_2) 3.8–11$\times10^{-33}$	3 10 1
*21.	$^3O + {}^3CH_2 + M \longrightarrow H_2CO + M$	6.7×10^{-11}	1.9–20$\times10^{-11}$	1	(N_2) 9.2×10^{-29} (CO_2) 1.1×10^{-28} (H_2) 1.7×10^{-28}		
*22.	$^3O + CH + M \longrightarrow HCO + M$	1.1×10^{-10}	6.6–9.5$\times10^{-11}$	1	(N_2) 5.2×10^{-30} (CO_2) 6.2×10^{-30} (H_2) 9.9×10^{-30}		
23.	$^3O + H + M \longrightarrow OH + M$	3.5×10^{-10}			(N_2) 2.6×10^{-33} (CO_2) 2.9×10^{-33} (H_2) 4.6×10^{-33}	(M) 1–8000$\times10^{-33}$ ” ”	1 1 1
*24.	$^1O + HCN + M \longrightarrow HCNO + M$	3.3×10^{-11}			(N_2) 4.0×10^{-29} (CO_2) 4.6×10^{-29} (H_2) 8.0×10^{-29}		
*25.	$^1O + CN + M \longrightarrow NCO + M$	8.9×10^{-11}			(N_2) 1.9×10^{-29} (CO_2) 2.1×10^{-29} (H_2) 3.6×10^{-29}		
*26.	$^1O + {}^1O + M \longrightarrow O_2 + M$	2.3×10^{-10}			(N_2) 8.8×10^{-33} (CO_2) 9.6×10^{-33} (H_2) 1.8×10^{-32}		
*27.	$^1O + CH_4 + M \longrightarrow CH_3OH + M$	5.8×10^{-9}	1.4–4.0$\times10^{-10}$	15	(N_2) 3.6×10^{-23} (CO_2) 3.9×10^{-23} (H_2) 6.3×10^{-23}		
*28.	$^1O + {}^1CH_2 + M \longrightarrow H_2CO + M$	3.3×10^{-10}			(N_2) 6.6×10^{-27} (CO_2) 7.7×10^{-27} (H_2) 1.2×10^{-26}		
*29.	$^1O + CH + M \longrightarrow HCO + M$	9.2×10^{-11}			(N_2) 4.9×10^{-29} (CO_2) 5.8×10^{-29} (H_2) 9.1×10^{-29}		

*30. $^1O + H_2 + M \longrightarrow H_2O + M$	7.1×10^{-10}	$1.1–3.0\times10^{-10}$	2	(N_2) 1.2×10^{-29} (CO_2) 1.4×10^{-29} (H_2) 2.0×10^{-29}
*31. $^1O + H + M \longrightarrow OH + M$	1.1×10^{-9}			(N_2) 1.4×10^{-32} (CO_2) 1.5×10^{-32} (H_2) 2.3×10^{-32}

∗ Reactions with no previously known rate coefficients.

Our calculated high-pressure rate coefficients are within the range of experimental values in 9 out of 12 cases. The other three rate coefficients are factors of 2, 5, and 15 from the nearest experimental values. Typical uncertainties for rate coefficients–as assigned in large experimental data evaluations–range from factors of 2–10[27,28]; Therefore, this calculated accuracy is consistent with the levels of uncertainty typically found in the literature.

Each low-pressure limit rate coefficient was calculated for three bath gases (N_2, CO_2, and H_2) and compared to experiments performed with matching bath gases when possible, and any bath gases otherwise. Nine of the reactions had experimentally measured low-pressure limit rate coefficients for one or more bath gases. All of our calculated rate coefficients for these reactions landed within an order of magnitude of the experimental range for the matching bath gas when possible, or another bath gas otherwise. Most commonly (67% of the time), our rate coefficients were within a factor of 3 from the nearest experimental measurement. Larger deviations tended to occur for cases that only have a single experimental measurement for comparison.

In Table 3, we display the 95 one- and two-body reaction rate coefficients calculated at 298K with any experimental or suggested values. 47 of these reactions have experimental or suggested values, and our calculations are within approximately one order of magnitude of these values in all but one case. In 60% of cases our calculated rate coefficients are within a factor of 2 of experimental values, and in 83% of cases our calculated rate coefficients are within a factor of 6 of experimental values.

In one case, $OH + CH_4 \longrightarrow H_2O + CH_3$, our calculated rate coefficient has a slightly higher than an order of magnitude deviation from experiment (factor of 54). We attribute this error to the lack of a quantum tunneling correction in our calculations. Bravo-Pérez et al.[55] performed transition state theory calculations for this reaction at the BHandHLYP/6-311G(d,p) level of theory, and calculated a tunneling factor of 30.56 at 298 K using an Eckart model. If we applied this factor to our calculation, our rate coefficient would be within a factor of two of the experimental range.

TABLE 3: Calculated reaction rate coefficients at 298 K for the one- and two-body reactions in this paper. Calculations are performed at the BHandHLYP/aug-cc-pVDZ level of theory. Reactions with rate coefficients slower than $k = 10^{-21}$ are not included in this network. The precense or absence of an energy barrier in the rate-limiting step (or the only step) of the reaction is specified. The error factor is the multiplicative or divisional factor from the nearest experimental or suggested value; the error factor is 1 if the calculated value is within the range of experimental or suggested values. First-order rate coefficients have units s^{-1}. Second-order rate coefficients have units cm^3s^{-1}.

No.	Reaction equation	Forw./Rev.	Barrier?	k(298) calculated	k(298) experimental	Error factor
*32.	$NCCO \longrightarrow CO + CN$	F	Y	9.4×10^{-12}		
33.	$CO_2 + {}^1O \longrightarrow {}^1CO_3\cdot \longrightarrow {}^3CO_3\cdot \longrightarrow CO_2 + {}^3O$	F	N	3.8×10^{-11}	$0.1–23\times10^{-11}$	1
34.	$CO_2 + {}^2N \longrightarrow NCO_2\cdot \longrightarrow OCNO\cdot \longrightarrow CO + NO$	F	[a]Y	3.2×10^{-14}	$1.8–6.8\times10^{-13}$	6
35.	$CO_2 + {}^1CH_2 \longrightarrow {}^1CH_2CO_2\cdot \longrightarrow H_2CO + CO$	F	N	8.0×10^{-13}		
36.	$CO_2 + CH \longrightarrow CHCO_2\cdot \longrightarrow HCOCO\cdot \longrightarrow HCO + CO$	F	[b]N	3.1×10^{-12}	$1.8–2.1\times10^{-12}$	1
37.	$H_2O_2 \longrightarrow OH + OH$	F	Y	5.1×10^{-9}		
38.	$H_2CO + CN \longrightarrow HCN + HCO$	F	N	1.7×10^{-11}	1.7×10^{-11}	1
39.	$H_2CO + OH \longrightarrow r,l\text{-}H_2COHO\cdot \longrightarrow trans\text{–}HCOHO\cdot + H\cdot \longrightarrow H_2O + CO + H$	F	Y	7.1×10^{-17}		
40.	$H_2CO + OH \longrightarrow H_2CO\cdots HO\cdot \longrightarrow H_2O + HCO$	F	Y	1.1×10^{-12}	$6.1–15\times10^{-12}$	6
41.	$H_2CO + {}^3O \longrightarrow HCO + OH$	F	Y	6.8×10^{-14}	$1.5–1.9\times10^{-13}$	2
*42.	$H_2CO + {}^1O \longrightarrow H_2CO_2\cdot \longrightarrow HCO_2H\cdot \longrightarrow HCO + OH$	F	N	4.6×10^{-10}		
43.	$H_2CO + CH_3 \longrightarrow HCO + CH_4$	F	Y	1.9×10^{-19}	$2.2–4.2\times10^{-18}$	12
44.	$H_2CO + {}^3CH_2 \longrightarrow HCO + CH_3$	F	Y	1.1×10^{-14}	$<1.0\times10^{-14}$	1
45.	$H_2CO + {}^1CH_2 \longrightarrow HCO + CH_3$	F	N	1.5×10^{-12}	2.0×10^{-12}	1

46.	$H_2CO + CH \longrightarrow H_2COCH_a \cdot \longrightarrow$ $H_2COCH_b \cdot \longrightarrow CH_2HCO \cdot \longrightarrow$ $CH_3CO \cdot \longrightarrow CO + CH_3$	F	N	3.1×10^{-11}	3.8×10^{-10}	12
47.	$H_2CO + CH \longrightarrow H_2COCH_c \cdot \longrightarrow$ $HCO + {}^3CH_2$	F	N	1.1×10^{-12}		
48.	$H_2CO + H \longrightarrow HCO + H_2$	F	Y	1.8×10^{-13}	$3.9–6.7\times10^{-14}$	3
*49.	$HCO + H_2CN \longrightarrow H_2CO + HCN$	F	Y	7.0×10^{-15}		
50.	$HCO + HCO \longrightarrow trans{-}C_2H_2O_2 \cdot \longrightarrow$ $anti{-}HCOH \cdot + CO \cdot \longrightarrow H_2CO + CO$	F	Y	1.2×10^{-13}	$2.8–750\times10^{-13}$	2
51.	$HCO + HCO \longrightarrow cis{-}C_2H_2O_2 \cdot \longrightarrow$ $CO + CO + H_2$	F	N	7.4×10^{-11}	3.6×10^{-11}	2
52.	$HCO + CN \longrightarrow HCOCN \cdot \longrightarrow CO + HCN$	F	N	5.4×10^{-12}		
53.	$HCO + OH \longrightarrow trans{-}HCOHO \cdot \longrightarrow CO + H_2O$	F	N	7.0×10^{-12}	$5–18\times10^{-11}$	7
54.	$HCO + {}^3O \longrightarrow HCO_2 \cdot \longrightarrow CO_2 + H$	F	N	2.6×10^{-11}	5.0×10^{-11}	2
55.	$HCO + {}^3O \longrightarrow CO + OH$	F	N	3.4×10^{-11}	5.0×10^{-11}	1
*56.	$HCO + {}^1O \longrightarrow HCO_2 \cdot \longrightarrow CO_2 + H$	F	N	1.5×10^{-10}		
*57.	$HCO + NH \longrightarrow H_2CO + {}^4N$	F	Y	3.6×10^{-20}		
*58.	$HCO + NH \longrightarrow CO + NH_2$ and $HCO + NH \longrightarrow HNHCO \cdot \longrightarrow H_2NCO \cdot \longrightarrow$ $CO + NH_2$	F	N	1.4×10^{-11}		
59.	$HCO + {}^4N \longrightarrow {}^3NCOH \cdot \longrightarrow NCO + H$	F	N	2.8×10^{-11}		
60.	$HCO + {}^4N \longrightarrow CO + NH$	F	N	2.2×10^{-11}		
*61.	$HCO + {}^2N \longrightarrow {}^3NCOH \cdot \longrightarrow NCO + H$	F	N	6.6×10^{-11}		
*62.	$HCO + {}^2N \longrightarrow CO + NH$	F	N	4.8×10^{-11}		
63.	$HCO + CH_3 \longrightarrow CO + CH_4$	F	N	1.0×10^{-11}	$3.6\times10^{-11}–2.0\times10^{-10}$	4
64.	$HCO + {}^3CH_2 \longrightarrow CH_3 + CO$ and $HCO + {}^3CH_2 \longrightarrow CH_2HCO \cdot \longrightarrow$ $CH_3CO \cdot \longrightarrow CH_3 + CO$	F	N	2.1×10^{-11}	3.0×10^{-11}	1
65.	$HCO + {}^1CH_2 \longrightarrow CH_2HCO \cdot \longrightarrow$ $CH_3CO \cdot \longrightarrow CH_3 + CO$	F	N	1.2×10^{-11}	3.0×10^{-11}	3
66.	$HCO + CH \longrightarrow CO + {}^3CH_2$	F	N	1.5×10^{-11}		
*67.	$HCO + CH \longrightarrow CO + {}^1CH_2$	F	N	4.6×10^{-12}		
68.	$HCO + H \longrightarrow CO + H_2$ and $HCO + H \longrightarrow H_2CO_{(\nu)} \cdot \longrightarrow CO + H_2$	F	N	6.9×10^{-11}	$1.1–5.5\times10^{-10}$	2
69.	$HCO + H \longrightarrow H_2CO_{(\nu)} \cdot \longrightarrow CO + H + H$	F	N	2.4×10^{-11}		
70.	$HCO \longrightarrow CO + H$	F	Y	2.2×10^{-2}		
71.	$CO + OH \longrightarrow OH\cdots CO \cdot \longrightarrow cis{-}HOCO \cdot \longrightarrow$ $CO_2 + H$	F	Y	$^c2.9\times10^{-12}$	$0.9–9.7\times10^{-13}$	3
72.	$H_2O + {}^1O \longrightarrow H_2OO \cdot \longrightarrow H_2O_2 \cdot \longrightarrow$ $OH + OH$	F	N	4.8×10^{-10}	$1.8–3.7\times10^{-10}$	1
73.	$H_2O + CN \longrightarrow H_2OCN \cdot \longrightarrow OH + HCN$	F	Y	6.6×10^{-15}		
74.	$H_2O + {}^2N \longrightarrow H_2ON \cdot \longrightarrow trans{-}HNOH \cdot \longrightarrow$ $HNO + H$ and $H_2O + {}^2N \longrightarrow H_2ON \cdot \longrightarrow trans{-}HNOH \cdot \longrightarrow$ $H_2NO \cdot \longrightarrow HNO + H$	F	N	1.9×10^{-10}		
75.	$H_2O + CH \longrightarrow H_2O\cdots CH \cdot \longrightarrow H_2OCH \cdot \longrightarrow$ $H_2COH \cdot \longrightarrow H_2CO + H$	F	^{d}N	2.0×10^{-10}	$1.3–4.5\times10^{-11}$	4
*76.	$H_2O + CH \longrightarrow OH + {}^3CH_2$	F	Y	3.9×10^{-16}		
77.	$OH + HCN \longrightarrow NCHOH \cdot \longrightarrow HOCN + H$	F	Y	1.2×10^{-15}	$0.1–31\times10^{-15}$	1
78.	$OH + CN \longrightarrow HO\cdots CN \longrightarrow {}^3HOCN_1 \cdot \longrightarrow$ $^3HOCN_2 \longrightarrow NCO + H$	F	Y	1.1×10^{-12}		
79.	$OH + CN \longrightarrow HCN + {}^3O$	F	Y	4.5×10^{-13}		
*80.	$OH + CN \longrightarrow HNC + {}^3O$	F	Y	2.3×10^{-17}		
81.	$OH + OH \longrightarrow trans{-}{}^3H_2O_2 \cdot \longrightarrow H_2O + {}^3O$	F	N	$^e2.5\times10^{-11}$	$0.8–2.6\times10^{-12}$	10
82.	$OH + {}^3O \longrightarrow HO_{2(\nu)} \cdot \longrightarrow O_2 + H$	F	N	7.4×10^{-11}	$2.8–4.2\times10^{-11}$	2
*83.	$OH + {}^1O \longrightarrow HO_{2(\nu)} \cdot \longrightarrow O_2 + H$	F	N	1.0×10^{-9}		
84.	$OH + NH \longrightarrow OH\cdots NH \cdot \longrightarrow trans{-}HNOH \cdot \longrightarrow$ $HNO + H$ and $OH + NH \longrightarrow OH\cdots NH \cdot \longrightarrow trans{-}HNOH \cdot \longrightarrow$ $H_2NO \cdot \longrightarrow HNO + H$	F	^{f}N	7.0×10^{-12}	3.3×10^{-11}	5
85.	$OH + NH \longrightarrow H_2O + {}^4N$	F	Y	6.8×10^{-13}	3.1×10^{-12}	5
86.	$OH + {}^4N \longrightarrow {}^3OH\cdots N \longrightarrow {}^3NOH \cdot \longrightarrow$	F	Y	1.0×10^{-10}	$4.2–5.3\times10^{-11}$	2

	$NO + H$					
*87.	$OH + {}^2N \longrightarrow {}^3OH\cdots N \longrightarrow {}^3NOH\cdot \longrightarrow$ $NO + H$	F	N	1.5×10^{-10}		
88.	$OH + CH_4 \longrightarrow H_2O + CH_3$	F	Y	1.1×10^{-16}	$5.9–11\times10^{-15}$	54
89.	$OH + CH_3 \longrightarrow {}^3O + CH_4$	F	Y	1.1×10^{-18}	1.8×10^{-17}	16
90.	$OH + CH_3 \longrightarrow H_2O + {}^3CH_2$	F	Y	3.5×10^{-18}		
91.	$OH + {}^3CH_2 \longrightarrow OH\cdots CH_2\cdot \longrightarrow H_2COH\cdot \longrightarrow$ $H_2CO + H$	F	N	4.6×10^{-11}	3.0×10^{-11}	2
92.	$OH + {}^3CH_2 \longrightarrow H_2O + CH$	F	N	7.6×10^{-13}		
93.	$OH + {}^1CH_2 \longrightarrow OH\cdots CH_2\cdot \longrightarrow H_2COH\cdot \longrightarrow$ $H_2CO + H$	F	N	4.6×10^{-11}	5.0×10^{-11}	1
94.	$OH + CH \longrightarrow {}^3OH\cdots CH\cdot \longrightarrow {}^3HCOH\cdot \longrightarrow$ ${}^3H_2CO\cdot \longrightarrow HCO + H$	F	N	3.2×10^{-11}		
95.	$OH + CH \longrightarrow anti{-}HCOH_{(\nu)}\cdot \longrightarrow$ $H_2CO_{(\nu)}\cdot \longrightarrow CO + H_2$	F	N	${}^g6.3\times10^{-12}$		
96.	$OH + CH \longrightarrow anti{-}HCOH_{(\nu)}\cdot \longrightarrow$ $H_2CO_{(\nu)}\cdot \longrightarrow CO + H + H$	F	N	${}^g6.3\times10^{-12}$		
97.	$OH + H_2 \longrightarrow H_2O + H$	F	Y	1.5×10^{-15}	$5.3–8.5\times10^{-15}$	4
98.	$OH + H \longrightarrow {}^3O + H_2$	F	Y	6.5×10^{-16}	$9.9\times10^{-17}–5.6\times10^{-16}$	1
*99.	${}^3O + H_2CN \longrightarrow CH_2NO\cdot \longrightarrow$ $HCNO + H$	F	Y	4.0×10^{-14}		
*100.	${}^3O + H_2CN \longleftarrow CH_2NO\cdot \longleftarrow$ $HCNO + H$	R	N	9.8×10^{-11}		
101.	${}^3O + H_2CN \longrightarrow CH_2NO\cdot \longrightarrow$ $HCNOH\cdot \longrightarrow OH + HCN$	F	Y	8.3×10^{-15}		
102.	${}^3O + HCN \longrightarrow {}^3NCOH \longrightarrow NCO + H$	F	Y	1.5×10^{-18}		
103.	${}^3O + HCN \longleftarrow {}^3NCOH \longleftarrow NCO + H$	R	Y	2.5×10^{-20}		
104.	${}^3O + CN \longrightarrow {}^4NCO \longrightarrow CO + {}^4N$	F	N	1.5×10^{-11}	$2.7\times10^{-12}–3.7\times10^{-11}$	1
105.	${}^3O + CN \longrightarrow NCO_{(\nu)} \longrightarrow CO + {}^2N$	F	N	7.1×10^{-12}	$9.4\times10^{-12}–1.6\times10^{-11}$	1
106.	${}^3O + NH \longrightarrow HNO\cdot \longrightarrow NO + H$	F	N	3.1×10^{-11}	5.0×10^{-11}	2
107.	${}^3O + NH \longrightarrow OH + {}^4N$	F	Y	2.2×10^{-14}	$<1.7\times10^{-13}–5.0\times10^{-12}$	1
108.	${}^3O + CH_4 \longrightarrow OH + CH_3$	F	Y	1.1×10^{-19}	$6.6\times10^{-19}–6.6\times10^{-16}$	6
109.	${}^3O + CH_3 \longrightarrow CH_3O\cdot \longrightarrow H_2CO + H$	F	N	9.4×10^{-11}	$>3.0\times10^{-11}–1.9\times10^{-10}$	1
110.	${}^3O + {}^3CH_2 \longrightarrow H_2CO_{(\nu)} \longrightarrow CO + H + H$	F	N	3.4×10^{-11}	${}^h1.0\times10^{-11}–1.0\times10^{-10}$	1
111.	${}^3O + {}^3CH_2 \longrightarrow H_2CO_{(\nu)} \longrightarrow CO + H_2$	F	N	3.4×10^{-11}	${}^h1.0\times10^{-11}–1.0\times10^{-10}$	1
*112.	${}^3O + {}^1CH_2 \longrightarrow {}^3H_2CO\cdot \longrightarrow HCO + H$	F	N	2.1×10^{-10}		
113.	${}^3O + CH \longrightarrow HCO_{(\nu)} \longrightarrow CO + H$	F	N	1.1×10^{-10}	6.6×10^{-11}	2
114.	${}^3O + CH \longrightarrow {}^4HCO\cdot \longrightarrow {}^4COH\cdot \longrightarrow$ $OH + C$	F	N	2.5×10^{-10}		
115.	${}^3O + H_2 \longrightarrow OH + H$	F	Y	7.2×10^{-19}	$7.0\times10^{-18}–1.1\times10^{-17}$	10
*116.	${}^1O + H_2CN \longrightarrow CH_2NO\cdot \longrightarrow$ ${}^3O + H_2CN$	F	Y	4.5×10^{-10}		
*117.	${}^1O + H_2CN \longrightarrow CH_2NO\cdot \longrightarrow$ $HCNO + H$	F	Y	6.0×10^{-13}		
*118.	${}^1O + H_2CN \longrightarrow CH_2NO\cdot \longrightarrow$ $HCNOH\cdot \longrightarrow HCN + OH$	F	Y	1.2×10^{-13}		
*119.	${}^1O + CN \longrightarrow NCO_{(\nu)} \longrightarrow CO + {}^2N$	F	N	8.9×10^{-11}		
120.	${}^1O + CH_4 \longrightarrow CH_3OH_{(\nu)} \longrightarrow OH + CH_3$	F	N	5.8×10^{-9}	$1.4–4.0\times10^{-10}$	15
*121.	${}^1O + CH_3 \longrightarrow CH_3O\cdot \longrightarrow H_2CO + H$	F	N	4.3×10^{-10}		
*122.	${}^1O + {}^3CH_2 \longrightarrow {}^3H_2CO\cdot \longrightarrow HCO + H$	F	N	7.0×10^{-10}		
*123.	${}^1O + {}^1CH_2 \longrightarrow H_2CO_{(\nu)} \longrightarrow$ $CO + H + H$	F	N	1.7×10^{-10}		
*124.	${}^1O + {}^1CH_2 \longrightarrow H_2CO_{(\nu)} \longrightarrow CO + H_2$	F	N	1.7×10^{-10}		
*125.	${}^1O + CH \longrightarrow HCO_{(\nu)} \longrightarrow CO + H$	F	N	9.2×10^{-11}		
126.	${}^1O + H_2 \longrightarrow H_2O_{(\nu)} \longrightarrow OH + H$	F	N	7.1×10^{-10}	$1.1–3.0\times10^{-10}$	2

[a] We introduce a barrier of 17.15 kJ mol^{-1} (half the HF barrier) to this calculation as no barrier is found at the BHandHLYP/aug-cc-pVDZ level of theory (see supplement for more details).

[b] We remove the barrier from this calculation as experiment predicts this reaction to be barrierless below 400 K[56].

[c] We remove the intermediate barriers from this reaction and reduce the barrierless first step by a factor of 3.4 to match the barrier effects at the B3LYP/aug-cc-pVDZ level of theory. Experiments predict this reaction to have little to no barrier[27].

[d] We remove the barrier from the rate limiting third step of this calculation, as experiment predicts this reaction to be barrierless[57].

[e] Simulations did not converge beyond a O-O bond distance of 2.90Å. The rate coefficient is calculated with the variational transition state at

this location, which has the highest ΔG.

[f] We remove the barrier from the rate limiting third step of this calculation, as data evaluations suggest little to no barrier for this reaction[58].

[g] This rate coefficient is one half of the calculated rate coefficient for $OH + CH \longrightarrow anti{-}HCOH_{(\nu)}\cdot$ as both $CO + H_2$ and $CO + H + H$ are equally probable decay pathways for $anti{-}HCOH_{(\nu)}$[27,28,59].

[h] Experimental values are for $^3O + {}^3CH_2 \longrightarrow$ products divided by 2. As both product channels $CO + H + H$ and $CO + H_2$ are suggested to be equally likely[27,28,59].

Method Limitations

Occasionally computational methods misdiagnose reaction energy barriers. In other words, a method may calculate a barrier when experiments suggest the reaction is barrierless, or a method may calculate no barrier when experiments suggest a small-to-modest-sized barrier (∼1–20 kJ mol^{-1}) exists. We find this to be biggest limitation of applying a consistent computational quantum method to a large number of reactions. This is the main reason for taking a hybrid approach to building CRAHCN-O. Experiments are the most accurate method to calculate rate coefficients, therefore experimental values will always be used when possible. However, for the large number of reactions without experimentally measured rate coefficients, we must use a robust and feasible computational method to calculate and include these reactions in the network.

In four cases (noted in Table 3), our chosen computational method (BHandHLYP/aug-cc-pVDZ) predicts barriers at the first step or an intermediate step of reactions that are expected to be barrierless. In one other case, this method predicts a reaction had no barrier, when experiment suggests a barrier of 17.15 kJ mol^{-1}[60]. For these few cases, we artificially remove the barriers from these calculations, or introduce an experimental barrier. Based on the calculations in this paper, we find this method correctly diagnoses barriers ∼92% of the time.

Comparing the barrier diagnosis capabilities of BHandHLYP/aug-cc-pVDZ with two other widely used method in past work[18], we find CCSD/aug-cc-pVTZ and ωB97XD/aug-cc-pVDZ share these limitations. For 11 chosen reactions, BHandHLYP/aug-cc-pVDZ misdiagnosed 4 barriers, CCSD/aug-cc-pVTZ misdiagnosed 5 barriers, and ωB97XD/aug-cc-pVDZ misdiagnosed 2 barriers.

A second limitation of our method is that we do not include a correction factor for quantum mechanical tunneling. This may not be a big concern at 298 K, where our rate coefficient calculations are typically within a factor of two of experimental values, and generally always within an order of magnitude of experimental values. However, tunneling is most relevant at lower temperatures[61].

Given the lack of experimental low temperature ($\lesssim$ 230 K) rate coefficient data for the reactions in this study, we cannot obtain a valid statistical sense of the accuracy of our method for calculating low temperature rate coefficients. However, it is a reasonable assumption that our treatment leads to larger uncertainties at the lower end of our temperature range (50–200 K), where tunneling plays a greater role; possibly up to two orders of magnitude.

DISCUSSION

Highlighted New Reactions

As we have already noted, we have discovered 45 previously unknown reactions and provide the first calculations of their rate coefficients. In Table 4, we highlight 6 of these reactions. These reactions are potentially key pathways for the production and destruction of HCN or H_2CO in planetary atmospheres due to their high rate coefficients at 298 K, and the reasonably high abundances of their reactants in atmospheres.

Different reactions tend to dominate in different regions of an atmosphere. In the diffuse upper atmosphere (thermosphere), incoming UV radiation breaks apart dominant atmospheric species to produce radicals. In the dense lower atmosphere (troposphere), radicals can be transported from the upper atmosphere via turbulent mixing, or produced by lightning and/or GCRs. In this lower region, there is also sufficient pressure to collisionally deexcite the vibrationally excited intermediates in three-body reactions.

One newly discovered reaction with a great potential to produce substantial amounts H_2CO in upper atmospheres is $^1O + CH_3 \longrightarrow H_2CO + H$. Firstly, there will likely be high concentrations of reactants ^1O and CH_3 in the upper atmospheres of planets containing CO_2 and CH_4, as the former are the direct photodissociation fragments of the latter. Secondly, this reaction has a barrierless rate coefficient of $k(298\text{ K}) = 4.3\times10^{-10}$ cm^{3}s^{-1}, which is in the 94th percentile for highest two-body reaction rate coefficients in this study. For these reasons, we expect this reaction to be a dominant source of H_2CO in CO_2-rich and CH_4-containing atmospheres such as the early Earth. At the CCSD/aug-cc-pVDZ level of theory, we calculate this rate coefficient to be only 14% lower (3.7×10^{-10} cm^{3}s^{-1}), suggesting this calculation is not very sensitive to the choice of computational method.

In lower planetary atmospheres, we find two new three-body reactions that may be important pathways to H_2CO. These reactions are $^1O + {}^1CH_2 + M \longrightarrow H_2CO + M$ and $^3O + {}^3CH_2 + M \longrightarrow H_2CO + M$. These reactions are most favourable at the high-pressure limit, where their rate coefficients are $k_\infty(298\text{ K}) = 3.3\times10^{-10}$ and 6.7×10^{-11} cm^{3}s^{-1}, respectively. The pressures at which these reaction rate coefficients reach 90% of $k_\infty(298\text{ K})$ in a N_2 bath gas are 0.61 bar and 7.1 bar, respectively.

TABLE 4. Highlighted newly discovered reactions in this work, listed with their calculated rate coefficients at 298 K and potential for importance in atmospheres. For simplicity, reaction intermediates are not listed here. See Tables 2 and 3 for full details of reaction intermediates. Second-order rate coefficients have units cm^3s^{-1}. Third-order rate coefficients have units cm^6s^{-1}.

Reaction	k(298) calculated	Importance
$^1O + CH_3 \longrightarrow H_2CO + H$	4.3×10^{-10}	H_2CO production in upper atmospheres
$^1O + {}^1CH_2 + M \longrightarrow H_2CO + M$	$k_\infty = 3.3\times10^{-10}$	H_2CO production in lower atmospheres
	$k_0(N_2) = 6.6\times10^{-27}$	
	$k_0(CO_2) = 7.7\times10^{-27}$	
	$k_0(H_2) = 1.2\times10^{-26}$	
$^3O + {}^3CH_2 + M \longrightarrow H_2CO + M$	$k_\infty = 6.7\times10^{-11}$	H_2CO production in lower atmospheres
	$k_0(N_2) = 9.2\times10^{-29}$	
	$k_0(CO_2) = 1.1\times10^{-28}$	
	$k_0(H_2) = 1.7\times10^{-28}$	
$^1O + H_2CN \longrightarrow HCN + OH$	1.2×10^{-13}	HCN production in upper atmospheres
$H_2CO + {}^1O \longrightarrow HCO + OH$	4.6×10^{-10}	H_2CO destruction in upper atmospheres
$^1O + HCN + M \longrightarrow HCNO + M$	$k_\infty = 3.3\times10^{-11}$	HCN destruction in lower atmospheres
	$k_0(N_2) = 4.0\times10^{-29}$	
	$k_0(CO_2) = 4.6\times10^{-29}$	
	$k_0(H_2) = 8.0\times10^{-29}$	

Such pressures would have been present in the evolving early Earth atmosphere ∼4.5 billion years ago[62].

For new potentially important routes to HCN, we find $^1O + H_2CN \longrightarrow HCN + OH$, which has a rate coefficient of $k(298\ K) = 1.2\times10^{-13}$ cm^3s^{-1}. This reaction has the potential to be an important source of HCN in upper atmospheres with high CO_2 mixing ratios, and low H_2 and CH_4 mixing ratios. The reason for this is that there is a direct competing reaction for HCN production from $H_2CN + H \longrightarrow HCN + H_2$, which has a rate coefficient of $k(298\ K) = 2.2\times10^{-11}$ cm^3s^{-1}. Therefore, the $^1O/H$ ratio in upper atmospheres will determine which of these two reactions dominates. We note also that this reaction has a complex reaction scheme, with two other favourable channels from the $H_2CNO\cdot$ intermediate: $HCNO + H$ and $^3O + H_2CN$. Our calculations of this reaction rate coefficient using two other computational methods (ωB97XD, CCSD) suggests the channel to $HCN + OH$ may be more favourable than our BHandHLYP calculation implies, by up to a factor of ∼700 (see theoretical case study 9 in the SI for more details). Given these discrepancies, and the novelty of this reaction, we recommend experimental measurements be performed for the three product channels of $^1O + H_2CN$.

A new reaction with a great potential to destroy H_2CO is $H_2CO + {}^1O \longrightarrow HCO + OH$, which has a barrierless rate coefficient of 4.6×10^{-10} cm^3s^{-1} at 298 K. As with the main new production pathway to H_2CO, this rate coefficient is one of the highest two-body rate coefficients in this study, and likely plays a role of attenuating H_2CO in upper atmospheres. At the CCSD/aug-cc-pVDZ level of theory, we calculate this rate coefficient to be only 50% lower (2.3×10^{-10} cm^3s^{-1}) than the value at the BHandHLYP/aug-cc-pVDZ level of theory.

Lastly, we highlight a new HCN destruction pathway in lower atmospheres, $^1O + HCN + M \longrightarrow HCNO + M$. This reaction may be particularly important in attenuating HCN abundances in the troposphere, which is the region where HCN dissolves in rain droplets and makes its way into surface water. This reaction rate coefficient reaches 90% of $k_\infty(298\ K)$ in a N_2 bath gas at 3 bar.

CRAHCN-O

CRAHCN-O is a chemical reaction network that can be used to simulate the production of HCN and H_2CO in atmospheres ranging from ∼50–400 K dominated by any of the following gases: CO_2, N_2, H_2O, CH_4, and H_2. CRAHCN-O is the amalgamation of the CRAHCN network developed in Pearce et al.[18] and the oxygen extension developed in this work. CRAHCN-O contains experimental rate coefficients (when available), and our consistently calculated theoretical rate coefficients from this work otherwise.

We summarize the oxygen extension in Tables S1 and S2 in the supplementary materials. In addition to the 126 reactions explored in this work, we include one experimental spin-forbidden collisionally induced intersystem crossing reaction ($^1O + M \longrightarrow {}^3O + M$), whose rate coefficient cannot be calculated using our theoretical method.

The original CRAHCN network can be found in the

appendices of Pearce et al.[18].

CONCLUSIONS

In this work, we use a novel technique making use of computational quantum chemistry and experimental data to build a consistent reduced atmospheric hybrid chemical network oxygen extension (CRAHCN-O). This network can be used to simulate HCN and H_2CO chemistry in planetary atmospheres dominated by CO_2, N_2, H_2O, CH_4, and H_2.

The oxygen extension contains 127 reactions, and is made up of approximately 30% experimental and 70% consistently calculated theoretical rate coefficients. Below are the main conclusions of this work in bullet point.

- We discover 45 previously unknown reactions, and are the first to calculate their rate coefficients. These new reactions typically involve electronically excited species (e.g., ^1O, $^1CH_2$, ^2N).
- The majority ($\sim$62%) of our calculated rate coefficients are accurate to within a factor of two of experimental measurements. $\sim$84% are accurate to within a factor of 6 of experimental values, and the rest are accurate to within about an order of magnitude of experimental values. This level of accuracy is consistent with the uncertainties assigned in large scale experimental data evaluations.
- We identify 6 potentially key new production and destruction pathways for H_2CO and HCN from these previously unknown reactions.
- The high, barrierless rate coefficient of $^1O + CH_3 \longrightarrow H_2CO + H$ (k(298 K) = 4.3×10^{-10} cm^3s^{-1}) likely makes it a key source of formaldehyde in upper atmospheres where ^1O and CH_3 are produced from the UV photodissociation of CO_2 and CH_4, respectively.
- Conversely, the high, barrierless rate coefficient of $H_2CO + {}^1O \longrightarrow HCO + OH$ (k(298 K) = 4.6×10^{-10} cm^3s^{-1}) likely makes it a key sink for formaldehyde in upper atmospheres.
- $^1O + H_2CN \longrightarrow HCN + OH$ is less efficient than the known HCN source, $H_2CN + H \longrightarrow HCN + H_2$; However the former may dominate HCN production in CO_2-rich upper atmospheres with high $^1O/H$ ratios from CO_2 photodissociation.
- In lower atmospheres (i.e. high partial pressures), H_2CO may form via new reactions between $^1O + {}^1CH_2$ and $^3O + {}^3CH_2$, which require a collisional third body at the high pressures present in these regions. HCN may be efficiently removed in this region via $^1O + HCN + M \longrightarrow HCNO + M$.

Having now filled in the missing chemical data relevant to HCN and H_2CO production in CO_2- and H_2O-rich atmospheres, we intend to couple CRAHCN-O to a 1D chemical kinetic model to simulate the atmosphere of the early Earth.

SUPPORTING INFORMATION

Rate coefficient data, experimental data, Lennard-Jones parameters, theoretical case studies, and quantum chemistry data.

ACKNOWLEDGMENTS

B.K.D.P. is supported by an NSERC Alexander Graham Bell Canada Graduate Scholarship-Doctoral (CGS-D). P.W.A is supported by NSERC, the Canada Research Chairs, and Canarie. R.E.P. is supported by an NSERC Discovery Grant. We acknowledge Compute Canada for allocating the computer time required for this research.

REFERENCES

[1] Oró, J. Mechanism of Synthesis of Adenine from Hydrogen Cyanide under Possible Primitive Earth Conditions. *Nature* **1961**, *191*, 1193–1194.
[2] Larowe, D. E.; Regnier, P. Thermodynamic Potential for the Abiotic Synthesis of Adenine, Cytosine, Guanine, Thymine, Uracil, Ribose, and Deoxyribose in Hydrothermal Systems. *Orig. Life Evol. Biosph.* **2008**, *38*, 383–397.
[3] Ferus, M. et al. Prebiotic synthesis initiated in formaldehyde by laser plasma simulating high-velocity impacts. *Astron. Astrophys.* **2019**, *626*, A52.
[4] Butlerow, A. Bildung einer zuckerartigen Substanz durch Synthese. *Ann. Chem. Pharm.* **1861**, *120*, 295–298.
[5] Breslow, R. On the mechanism of the formose reaction. *Tetrahedron Letts.* **1959**, *1*, 22–26.
[6] Strecker, A. Ueber einen neuen aus AldehydAmmoniak und Blausäure entstehenden Körper. *Liebigs Ann. Chem.* **1854**, *91*, 349–351.
[7] Miller, S. L.; Van Trump, J. E. In *Origin of Life*; Wolman, Y., Ed.; Reidel: Dordrecht, The Netherlands, 1981; pp 135–141.
[8] Catling, D.; Kasting, J. F. In *Planets and life - the emerging science of astrobiology*; Sullivan, III, W. T.,

Baross, J. A., Eds.; Cambridge University Press: Cambridge, 2007; pp 91–116.

[9] Trail, D.; Watson, E. B.; Tailby, N. D. The oxidation state of Hadean magmas and implications for early Earths atmosphere. *Nature* **2011**, *480*, 79–82.

[10] Pinto, J. P.; Gladstone, G. R.; Yung, Y. L. Photochemical Production of Formaldehyde in Earth's Primitive Atmosphere. *Science* **1980**, *210*, 183–185.

[11] Schmidt, J. A.; Johnson, M. S.; Schinke, R. Carbon dioxide photolysis from 150 to 210 nm: Singlet and triplet channel dynamics, UV-spectrum, andisotope effects. *Proc. Nat. Acad. Sci. U.S.A.* **2013**, *110*, 17691–17696.

[12] Shi, X.; Yin, Q.-Z.; Gao, H.; Chang, Y.-C.; Jackson, W. M.; Wiens, R. C.; Ng, C.-Y. Branching Ratios in Vacuum Ultraviolet Photodissociation of CO and N_2: Implications for Oxygen and Nitrogen Isotopic Compositions of the Solar Nebula. *Astrophys. J.* **2017**, *850*, 48.

[13] Gans, B.; Boyé-Péronne,, S.; Broquier, M.; Delsaut, M.; Douin, S.; Fellows, C. E.; Halvick, P.; Loison, J.-C.; Lucchese, R. R.; Gauyacq, D. Photolysis of methane revisited at 121.6 nm and at 118.2 nm: quantum yields of the primary products, measured by mass spectrometry. *Phys. Chem. Chem. Phys.* **2011**, *13*, 8140–8152.

[14] Engel, V.; Staemmler, V.; Vander Wal, R. L.; Crim, F. F.; Sension, R. J.; Hudson, B.; Andreson, P.; Hennig, S.; Weide, K.; Schinke, R. Photodissociation of water in the first absorption band: a prototype for dissociation on a repulsive potential energy surface. *J. Phys. Chem.* **1992**, *96*, 3201–3213.

[15] Stecher, T. P.; Williams, D. A. Photodestruction of Hydrogen Molecules in H I Regions. *Astrophys. J. Lett.* **1967**, *149*, L29.

[16] Zahnle, K. J. Photochemistry of Methane and the Formation of Hydrocyanic Acid (HCN) in the Earth's Early Atmosphere. *J. Geophys. Res.* **1986**, *91*, 2819–2834.

[17] Tian, F.; Kasting, J. F.; Zahnle, K. Revisiting HCN formation in Earth's early atmosphere. *Earth Planet. Sci. Lett.* **2011**, *308*, 417–423.

[18] Pearce, B. K. D.; Molaverdikhani, K.; Pudritz, R. E.; Henning, T.; Hébrard, E. HCN production in Titan's Atmosphere: Coupling quantum chemistry and disequilibrium atmospheric modeling. *Astrophys. J, in press* **2020**,

[19] Pearce, B. K. D.; Ayers, P. W.; Pudritz, R. E. A Consistent Reduced Network for HCN Chemistry in Early Earth and Titan Atmospheres: Quantum Calculations of Reaction Rate Coefficients. *J. Phys. Chem. A* **2019**, *123*, 1861–1873.

[20] Truhlar, D. G.; Garrett, B. C. Variational Transition State Theory. *Annu. Rev. Phys. Chem.* **1984**, *35*, 159–189.

[21] Forst, W. *Unimolecular Reactions: A Concise Introduction*; Cambridge University Press: Cambridge, U.K., 2003.

[22] Becke, A. D. A new mixing of Hartree-Fock and local density-functional theories. *J. Chem. Phys.* **1993**, *98*, 1372–1377.

[23] Lee, C.; Yang, W.; Parr, R. G. Development of the Colle-Salvetti correlation-energy formula into a functional of the electron density. *Phys. Rev. B* **1988**, *37*, 785–789.

[24] Dunning, Jr., T. H. Gaussian basis sets for use in correlated molecular calculations. I. The atoms boron through neon and hydrogen. *J. Chem. Phys.* **1989**, *90*, 1007–1023.

[25] Kendall, R. A.; Dunning, Jr., T. H. Electron affinities of the firstrow atoms revisited. Systematic basis sets and wave functions. *J. Chem. Phys.* **1992**, *96*, 6796–6806.

[26] Woon, D. E.; Dunning, Jr., T. H. Gaussian-basis sets for use in correlated molecular calculations. 3. The atoms aluminum through argon. *J. Chem. Phys.* **1993**, *98*, 1357–1371.

[27] Baulch, D. L.; Cobos, C. J.; Cox, R. A.; Esser, C.; Frank, P.; Just, T.; Kerr, J. A.; Pilling, M. J.; Troe, J.; Walker, R. W.; et al., Evaluated kinetic data for combustion modelling. *J. Phys. Chem. Ref. Data* **1992**, *21*, 411–429.

[28] Tsang, W.; Hampson, R. F. Chemical Kinetic Data Base for Combustion Chemistry. Part I. Methane and Related Compounds. *J. Phys. Chem. Ref. Data* **1986**, *15*, 1087–1279.

[29] Frisch, M. J.; Trucks, G. W.; Schlegel, H. B.; Scuseria, G. E.; Robb, M. A.; Cheeseman, J. R.; Scalmani, G.; Barone, V.; Petersson, G. A.; Nakatsuji, H.; et al., *Gaussian 09*, Revision E.01; Gaussian, Inc.: Wallingford, CT, 2009.

[30] Avogadro: an open-source molecular builder and visualization tool. Version 1.2.0. http://avogadro.cc/.

[31] Hanwell, M. D.; Curtis, D. E.; Lonie, D. C.; Vandermeersch, T.; Zurek, E.; Hutchison, G. R. Avogadro: An advanced semantic chemical editor, visualization, and analysis platform. *J. Cheminform.* **2012**, *4*, 17.

[32] Truhlar, D. G. In *Theory of Chemical Reaction Dynamics*; Baer, M., Ed.; CRC Press: Boca Raton, FL, 1985; pp 65–137.

[33] Truhlar, D. G.; Garrett, B. C. Variational Transition-State Theory. *Acc. Chem. Res.* **1980**, *13*, 440–448.

[34] Eyring, H. The Activated Complex in Chemical Reactions. *J. Chem. Phys.* **1935**, *3*, 107.

[35] Vallance, C. *An Introduction to Chemical Kinetics*; 2053-2571; Morgan & Claypool Publishers: San Rafael, CA, 2017.

[36] Carstensen, H.-H.; Dean, A. M. In *Comprehensive Chemical Kinetics*; Carr, R., Ed.; Elsevier: Amsterdam, 2007; Vol. 42; pp 101–184.

[37] Barker, J. R.; Nguyen, T. L.; Stanton, J. F.; Aieta, C.; Ceotto, M.; Gabas, F.; Kumar, T. J. D.; Li, C. G. L.; Lohr, L. L.; Maranzana, A.; Ortiz, N. F.; Preses, J. M.; Simmie, J. M.; Sonk, J. A.; Stimac, P. J. *MultiWell-2019 Software Suite*; J. R. Barker: University of Michigan Ann Arbor, Michigan, USA, 2019.

[38] Barker, J. R. MultipleWell, multiplepath unimolecular reaction systems. I. MultiWell computer program suite. *Int. J. Chem. Kinet.* **2001**, *33*, 232–245.

[39] Barker, J. R. Energy transfer in master equation simulations: A new approach. *Int. J. Chem. Kinet.* **2009**, *41*, 748–763.

[40] Pilling, M. J.; Robertson, S. H. Master Equation Models for Chemical Reactions of Importance in Combustion. *Annu. Rev. Phys. Chem.* **2003**, *54*, 245–275.

[41] Akbar Ali, M.; Barker, J. R. Comparison of Three Isoelectronic Multiple-Well Reaction Systems: $OH + CH_2O$, $OH + CH_2CH_2$, and $OH + CH_2NH$. *J. Phys. Chem. A* **2015**, *119*, 7578–7592.

[42] Gong, C.-M.; Ning, H.-B.; Li, Z.-R.; Li, X.-Y. Theoretical and kinetic study of reaction $C_2H + C_3H_6$ on the C_5H_7 potential energy surface. *Theor. Chem. Acc.* **2015**, *134*, 1599.

[43] Zhao, L.; Ye, L.; Zhang, F.; Zhang, L. Thermal Decomposition of 1Pentanol and Its Isomers: A Theoretical Study.

J. Phys. Chem. A. **2012**, *116*, 9238–9244.

[44] Reid, R. C.; Prausnitz, J. M.; Sherwood, T. K. *The Properties of Gases and Liquids, Third Edition*; McGraw-Hill, Inc: New York, 1977; p 683.

[45] Welty, J. R.; Wicks, C. E.; Wilson, R. E.; Rorrer, G. L. *Fundamentals of Momentum, Heat, and Mass Transfer, 5th Edition*; John Wiley & Sons, Inc.: Hoboken, NJ, 2008; p 711.

[46] Wang, H.; Dames, E.; Sirjean, B.; Sheen, D. A.; Tango, R.; Violi, A.; Lai, J. Y. W.; Egolfopoulos, F. N.; Davidson, D. F.; Hanson, R. K.; et al., *JetSurF version 2.0*; 2010.

[47] Clary, D. C. Fast Chemical Reactions: Theory Challenges Experiment. *Annu. Rev. Phys. Chem.* **1990**, *41*, 61–90.

[48] Li, H.; Chen, B.-Z.; Huang, M.-B. CASPT2 investigation of ethane dissociation and methyl recombination using canonical variational transition state theory. *Int. J. Chem. Kinet.* **2008**, *40*, 161–173.

[49] Hase, W. L.; Mondro, S. L.; Duchovic, R. J.; Hirst, D. M. Thermal Rate Constant for $H + CH_3 \longrightarrow CH_4$ Recombination. 3. Comparison of Experiment and Canonical Variational Transition State Theory. *J. Am. Chem. Soc.* **1987**, *109*, 2916–2922.

[50] Jasper, A. W.; Klippenstein, S. J.; Harding, L. B. Secondary Kinetics of Methanol Decomposition: Theoretical Rate Coefficients for $^3CH_2 + OH$, $^3CH_2 + {}^3CH_2$, and $^3CH_2 + CH_3$. *J. Phys. Chem. A* **2007**, *111*, 8699–8707.

[51] Daranlot, J.; Hu, X.; Xie, C.; Loison, J.-C.; Caubet, P.; Costes, M.; Wakelam, V.; Xie, D.; Guo, H.; Hickson, K. Low temperature rate constants for the $N(^4S) + CH(X^2\Pi_r)$ reaction. Implications for N_2 formation cycles in dense interstellar clouds. *Phys. Chem. Chem. Phys.* **2013**, *15*, 13888–13896.

[52] Caldwell, J.; Back, R. A. Combination reactions of hydroxyl radicals in the flash photolysis of water vapour. *Trans. Faraday Soc.* **1965**, *61*, 1939–1945.

[53] Black, G.; Porter, G. Vacuum ultra-violet flash photolysis of water vapour. *Proc. R. Soc. Lond. A Math. Phys. Sci.* **1962**, *266*, 185–197.

[54] Zellner, R.; Erler, K.; Field, D. Kinetics of the recombination reaction OH + H + M $\rightarrow$ H_2O + M at low temperatures. Sixteenth Symposium (International) on Combustion. Seattle, 1977; pp 939–948.

[55] Bravo-Pérez, G.; Alvarez-Idaboy, J. R.; Jiménez, A. G.; Cruz-Torres, A. Quantum chemical and conventional TST calculations of rate constants for the OH + alkane reaction. *Chem. Phys.* **2005**, *310*, 213–223.

[56] Mehlmann, C.; Frost, M. J.; Heard, D. E.; Orr, B. J.; Nelson, P. F. Rate constants for removal of CH(D) (ν = 0 and 1) by collisions with N_2, CO, O_2, NO and NO_2 at 298 K and with CO_2 at $296 \leq T/K \leq 873$. *J. Chem. Soc., Faraday Trans.* **1996**, *92*, 2335–2341.

[57] Blitz, M. A.; Pesa, M.; Pilling, M. J.; Seakins, P. W. Reaction of CH with H2O:Temperature Dependence and Isotope Effect. *J. Phys. Chem. A* **1999**, *103*, 5699–5704.

[58] Cohen, N.; Westberg, K. R. Chemical Kinetic Data Sheets for High-Temperature Reactions. Part II. *J. Phys. Chem. Ref. Data* **1991**, *20*, 1211–1311.

[59] Schaub, W. M.; Hsu, D. S. Y.; Lin, M. C. Dynamics and mechanisms of CO production from the reactions of CH_2 radicals with $O(^3P)$ and O_2. Eighteenth Symposium (International) on Combustion. Seattle, 1981; pp 811–818.

[60] Husain, D.; Mitra, S. K.; Young, A. N. Kinetic Study of Electronically Excited Nitrogen Atoms, $N(2^2D_J,2^2P_J)$, by Attenuation of Atomic Resonance Radiation in the Vacuum Ultra-violet. *J. Chem. Soc., Faraday Trans. 2* **1974**, *70*, 1721–1731.

[61] Meisner, J.; Kästner, J. Atom Tunneling in Chemistry. *Angew Chem Int Ed Engl* **2016**, *55*, 5400–5413.

[62] Zahnle, K.; Arndt, N.; Cockell, C.; Halliday, A.; Nisbet, E.; Selsis, F.; Sleep, N. H. Emergence of a Habitable Planet. *Space Sci Rev* **2007**, *129*, 35–78.

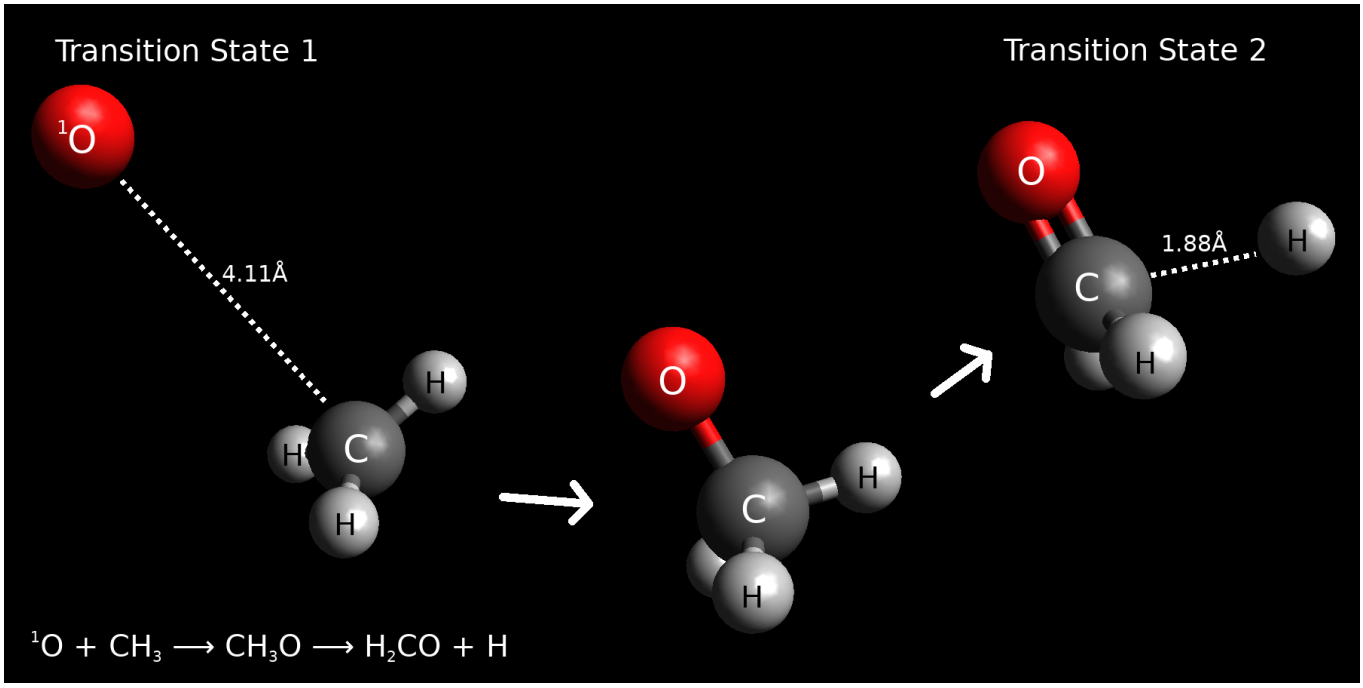

FIG. 1. TOC graphic